Photoacoustics 41 (2025) 100678

Contents lists available at ScienceDirect

Photoacoustics

journal homepage: www.elsevier.com/locate/pacs

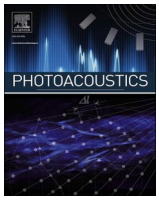

Temperature dependence of femtosecond photoacoustic process in high-precision characterization for metal nanofilms

Zhongyu Wang [a], Jing Min [a], Yong Sun [a], Xuesong Wang [a], Xiuguo Chen [a,b], Zirong Tang [a,b,*], Shiyuan Liu [a,b,*]

[a] School of Mechanical Science and Engineering, Huazhong University of Science and Technology, Wuhan 430074, China
[b] Optics Valley Laboratory, Wuhan 430074, China

ARTICLE INFO

Keywords:
Femtosecond photoacoustic
Metal nanofilms
Critical point model
Dynamic behavior
Optical properties

ABSTRACT

Femtosecond photoacoustic detection is a powerful all-optical technique for characterizing metal nanofilms. However, the lack of accurate descriptions of the temperature-dependent optical properties of metal nanofilms during ultrafast thermal processes hinders the deep understanding of this dynamic behavior, leading to compromised measurement accuracy. To address this, we developed Critical Point Models (CPMs) for copper and AlCu nanofilms to describe their dynamic optical properties during photoacoustic testing. By integrating dynamic behavior into ultrafast laser-matter interaction and acousto-optic processes, we explored the temperature effects throughout testing. Numerical simulations were performed to analyze the temperature, stress, and surface reflectivity distributions of the nanofilms. Compared to experimental results, our dynamic models significantly improved prediction accuracy for both copper and AlCu nanofilms. This highlights the importance of temperature dependence in femtosecond photoacoustic testing and validates our model's capability to capture the behavior of metal nanofilms under ultrafast laser irradiation.

1. Introduction

Metal nanofilms play a vital role in integrated circuits, new energy technologies, and sensors due to their exceptional properties, including electrical and thermal conductivity, reflectivity, and catalytic activity. These unique characteristics make them indispensable in advancing technology and industry. Accurate characterization of their properties is essential for ensuring reliable performance in both research and industrial applications. Femtosecond photoacoustic testing has emerged as a leading method for the characterization of opaque metal nanofilms, offering significant advantages such as high resolution, sensitivity, and non-destructive measurement capabilities[1,2]. This technique employs ultrafast pump pulses to excite high-frequency acoustic waves (up to hundreds of GHz) and captures these waves with probe pulses, enabling high-precision, non-contact, all-optical measurements[3].

However, in femtosecond photoacoustic testing, the measurement process is dynamic. The non-uniformly distributed and rapidly changing temperature field, induced by ultrafast laser irradiation, along with its diffusion process in the material, continuously affects the thermophysical and optical properties of the nanofilm. The dynamic behavior of these properties, in turn, influences the photoacoustic testing process, particularly the ultrafast laser-matter interaction and acousto-optic detection[4]. Ignoring this dynamic behavior will compromise the deep understanding of femtosecond photoacoustic testing. Therefore, an accurate predictive method for the temperature-dependent thermophysical and optical properties of metal nanofilms is essential. Additionally, a comprehensive measurement model that includes the dynamic process is crucial. Such a model can predict experimental outcomes under diverse lighting conditions and with different metal types. This is particularly beneficial for optimizing laser parameters for different metal nanofilms. For complex nanostructures, a precise model can minimize the resources required for data collection, which is critical for the efficacy of deep learning recognition methods[5].

Understanding thermophysical properties in ultrafast laser-matter interactions has advanced significantly. The Two-Temperature Model (TTM), first proposed by Anisimov[6], has been widely used and modified[7–10] to describe the non-equilibrium heating process in these interactions. The electron thermal conductivity during ultrafast laser-matter interactions is calculated using a semiempirical formula by Anisimov and Rethfeld[11]. Later, Migdal et al. proposed an approach

* Corresponding authors at: School of Mechanical Science and Engineering, Huazhong University of Science and Technology, Wuhan 430074, China.
E-mail addresses: zirong@hust.edu.cn (Z. Tang), shyliu@hust.edu.cn (S. Liu).

https://doi.org/10.1016/j.pacs.2024.100678
Received 13 August 2024; Received in revised form 28 November 2024; Accepted 9 December 2024
Available online 11 December 2024

combining first-principle calculations with analytical models to determine the heat conductivity of copper nanofilms[12]. The electron heat capacity and the electron-phonon coupling factor were calculated by Lin and Zhigilei based on the electron density of states[13]. For the optical properties of metal materials under laser irradiation, significant efforts have been made. The Drude model, including the Fermi smearing effect, was utilized to calculate the surface reflectivity and absorption coefficients under different temperature fields by Eesley[14]. Later, Fisher et al. modified the Drude model by considering both interband and intraband contributions in laser absorption to achieve a more precise evaluation of the surface reflectivity and absorption coefficients in copper and aluminum[15,16]. To account for the contribution of bound electrons to the electromagnetic wave response, Powell enhanced the Drude model by introducing Lorentz oscillators, leading to the development of the Lorentz-Drude Model (LDM) [17]. Building on this, Rakic et al. used LDM with multiple Lorentz oscillators to fit the optical property curves of various metals[18]. Furthermore, to address the inaccuracy of LDM when the laser wavelength approaches the absorption peak of the metal material, Etchegoin et al. introduced the critical point analysis of interband transitions to study the temperature-dependent optical properties of gold[19]. Based on this critical point model (CPM), Tsibidis calculated the thermomechanical response and damage threshold of gold[20]. Later, the CPMs were demonstrated to achieve greater accuracy in describing the permittivity of gold and silver compared to LDMs by Vial and Laroche[21]. For the application of CPM in copper, Ren et al. investigated the optical properties of copper under varying temperature fields using a critical point model that included three Lorentzian terms[22]. These studies highlight the importance of considering temperature-dependent properties during ultrafast laser-matter interactions.

Despite these advancements, research on temperature-dependent dynamic processes under ultrafast laser irradiation has mainly focused on ultrafast laser processing with high-intensity light sources[23]. Only a few types of metal materials have established corresponding CPMs, and there is a lack of study on introducing CPM into photoacoustic non-destructive testing using low-intensity lasers as light sources. Most studies emphasize the dynamic processes during ultrafast laser-matter interactions[24]. However, this is only one part of the comprehensive measurement model needed for femtosecond photoacoustic testing. The model must also account for the propagation and detection of acoustic waves. Few studies have considered the impact of temperature-dependent properties in these latter processes, resulting in less accurate measurement models and limiting the broader application of photoacoustic methods.

To address these limitations, we developed a dynamic model that fully accounts for the dynamic behavior of metal nanofilms throughout femtosecond photoacoustic testing. We introduced a CPM with three Lorentzian terms specifically designed for copper nanofilms and another CPM with four Lorentzian terms tailored for AlCu nanofilms (composed of 95 % aluminum and 5 % copper). After validating these models with experimental data, we integrated the CPMs into a measurement model that includes the TTM for ultrafast laser-matter interaction and the acousto-optic processes for pump-probe detection. We then conducted numerical simulations to analyze the entire testing process, focusing on temperature, stress, and surface reflectivity distribution of the nanofilms. The numerical results of dynamic model, when compared with experimental signals, show a significant improvement in accuracy across various laser parameters and nanofilm materials. This advancement represents a substantial leap in the accuracy of measurement models for photoacoustic detection, paving the way for more reliable diagnostics of metal nanofilms.

2. Theoretical framework

In femtosecond photoacoustic testing, the pump-probe technique is widely used to generate high-frequency acoustic waves. In this method, a femtosecond laser pulse (pump) first excites the metal nanofilm, creating a non-uniform temperature distribution and generating acoustic waves. A subsequent probe pulse, delayed by a controlled time interval, then interrogates the nanofilm to produce a time-domain curve with characteristic features. The schematics of femtosecond photoacoustic testing and pump-probe detection are shown in Fig. 1. This unique all-optical technique enables researchers to capture time-dependent dynamics on the femtosecond timescale, significantly improving the measurement accuracy of femtosecond photoacoustic testing.

To gain a deeper understanding of the ultrafast dynamic processes during this all-optical testing, it's essential to develop a theoretical model that fully considers the temperature-dependent properties of metal nanofilms. Therefore, we propose corresponding CPMs for copper and AlCu nanofilms to accurately describe the dynamic behavior of their optical parameters under varying temperature conditions.

2.1. Critical point models for metal nanofilms

When the laser wavelength gets close to a metal's absorption peak, where interband transitions are dominant, the accuracy of the LDM decreases. To overcome this limitation, we introduce critical point analysis of interband transitions. The critical point refers to the energy level in a metal where the probability of an interband transition changes significantly, usually corresponding to the top or bottom of the band structure. This point is essential for determining the material's optical properties. Unlike the LDM, the CPM provides a deeper understanding of how interband transitions affect the optical properties of materials. CPM has been successfully applied to gold, silver, and copper, showing good accuracy in predicting their optical properties[19–21].

A critical point model with three Lorentzian terms for copper and a critical point model with four Lorentzian terms for AlCu are proposed to evaluate the temperature-dependent optical properties of nanofilms during photoacoustic testing. The CPM can be expressed as[25]:

$$\varepsilon(\omega) = \varepsilon_\infty - \frac{{\omega_p}^2}{\omega^2 + i\Gamma\omega} + \sum_{j=1}^{n} G_j \tag{1}$$

$$G_j = A_j\omega_j\left(e^{i\phi_j}\left(\omega_j - \omega - i\Gamma_j\right)^{\mu_j} + e^{-i\phi_j}\left(\omega_j + \omega + i\Gamma_j\right)^{\mu_j}\right) \tag{2}$$

where ε_∞ is the high-frequency limit dielectric constant, ω_p is the plasma frequency, Γ is the damping term equal to the reciprocal of electron relaxation time (τ_e), n is the number of oscillators, A_j is the dimensionless critical point amplitude, ω_j is the energy of gap, ϕ_j is the phase, Γ_j is the broadening and the μ_j represents the order of the pole. In Eq. (1), the first two terms represent the contribution of the traditional Drude model, while the last term represents the interband transitions described by critical point analysis for a finite frequency range.

The order of the poles (μ_j) is typically determined for each gap to satisfy the dimensionality of the Van Hove singularity in the joint density of states for the interband transitions[26]. However, many features in the dielectric functions can be represented equally well by poles of different orders. A practical approach is to start with the simplest order poles until the desired accuracy is achieved, since the meanings and values of ω_j and Γ_j will not change significantly based on the exact choice of μ_j[19].

For the CPM used in this paper, both for copper and AlCu nanofilms, we chose $\mu_j = -1$ and achieved satisfactory fitting accuracy with the experimental results. Based on this choice, the full critical point model can be written as:

$$\begin{aligned}\varepsilon(\omega) &= \varepsilon_\infty - \frac{{\omega_p}^2}{\omega^2 + i\Gamma\omega} + \sum_{j=1}^{n} A_j\omega_j\left(\frac{e^{i\phi_j}}{\omega_j - \omega - i\Gamma_j} + \frac{e^{-i\phi_j}}{\omega_j + \omega + i\Gamma_j}\right) \\ &= \varepsilon_1 + i\varepsilon_2\end{aligned} \tag{3}$$

where ε_1 and ε_2 represent the real and imaginary parts of the dielectric

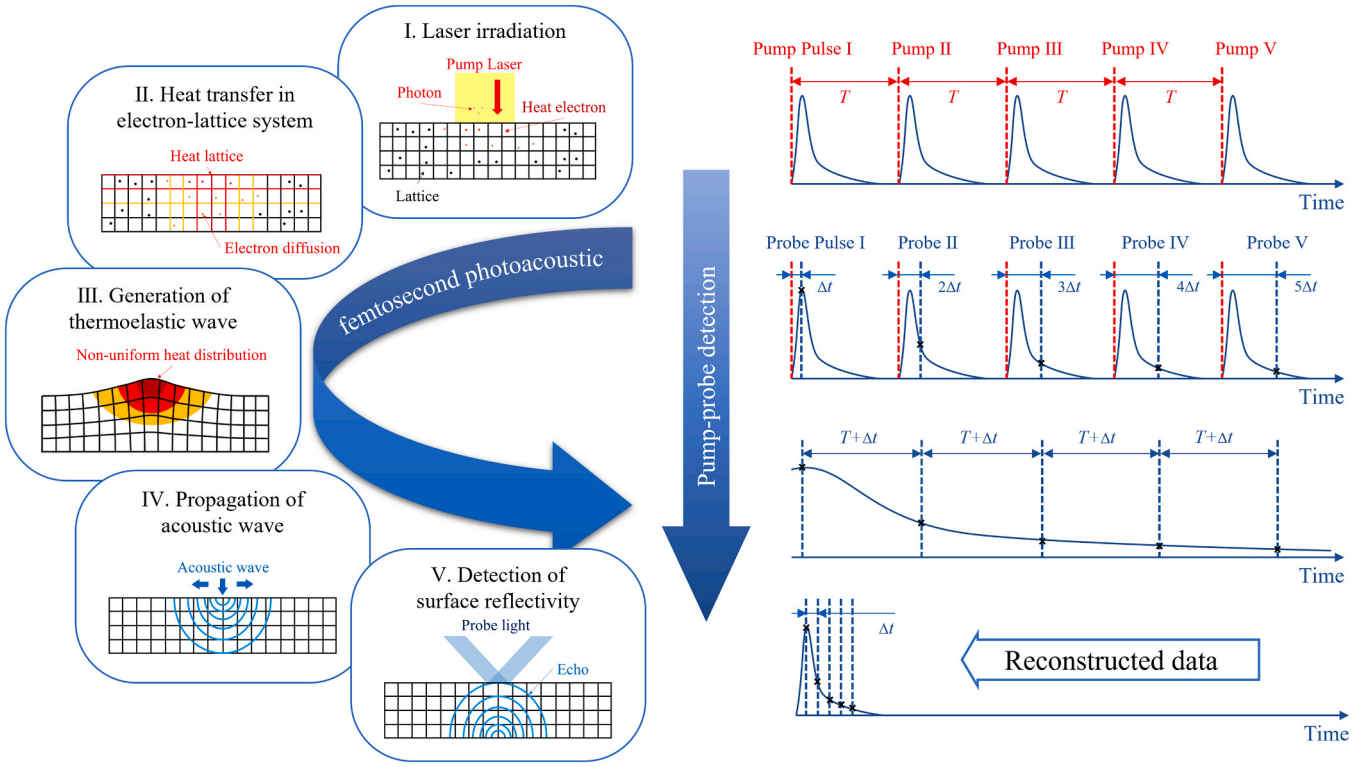

Fig. 1. Schematic of femtosecond photoacoustic pump-probe detection.

function, respectively. The parameters in Eq. (3) for different metal nanofilms are determined by simulated annealing method[27], and the fitting results will be presented and discussed later in Section 3.

To incorporate the effect of rapid behaviors in electron and lattice temperatures into the measurement model, the damping term Γ in the CPM under various temperature conditions can be expressed as:

$$\Gamma = \frac{1}{\tau_e} = \nu_{e-ph}(T_e, T_l) + \nu_{e-e}(T_e) \tag{4}$$

where ν_{e-ph} and ν_{e-e} are the electron momentum relaxation rates due to electron-phonon and electron-electron collisions, respectively.

Since photoacoustic testing is a non-destructive process, the laser intensity is relatively low, and the electron temperature will be significantly lower than the Fermi temperature of the material. In this situation ($K_B T_e \ll E_F$), ν_{e-ph} can be written as[15]:

$$\nu_{e-ph}(T_e, T_l) = \frac{\Xi^2}{8\pi E_F k_F \rho s}\frac{m_{opt}}{m_e} \times \left\{ \int_0^{q_b} \frac{e^{\phi_i}+e^{\phi_e}}{(e^{\phi_i}-1)(e^{\phi_e}+1)} q^4 dq + \eta \int_0^{q_b} \frac{e^{\phi_i}-e^{\phi_e}}{(e^{\phi_i}-1)(e^{\phi_e}+1)} q^3 dq + q_b \times \frac{e^{\varphi_i}+e^{\varphi_e}}{(e^{\varphi_i}-1)(e^{\varphi_e}+1)} \frac{(2k_F)^4 - {q_b}^4}{4} - \eta \times \frac{e^{\varphi_i}-e^{\varphi_e}}{(e^{\varphi_i}-1)(e^{\varphi_e}+1)} {q_b}^2 (2k_F)^2 \right\} \tag{5}$$

where $\phi_i = \beta_i \hbar q s$, $\phi_e = \beta_e \hbar q s$, $\varphi_i = \beta_i \hbar q_b s$, $\varphi_e = \beta_e \hbar q_b s$, $\beta_i = (K_B T_l)^{-1}$, $\beta_e = (K_B T_e)^{-1}$, Ξ is the deformation potential constant, E_F is the Fermi energy, k_F is the Fermi wave vector, ρ is the density, s is the longitudinal sound velocity, m_{opt} is the effective mass, m_e is the mass of a single electron, q is the phonon wave vector, and q_b is a constant determined by fitting Γ to the DC conductivity data.

For the second term on the right-hand side of Eq. (4), when $K_B T_e \lesssim E_F$, $\nu_{e-e}(T_e)$ can be written as[6]:

$$\nu_{e-e}(T_e) \approx \frac{E_F}{\hbar}\left(\frac{K_B T_e}{E_F}\right)^2 \tag{6}$$

The complex refraction index ($n + i\kappa$) of metal nanofilms can be calculated as[18]:

$$n = \left[\frac{\varepsilon_1 + (\varepsilon_1{}^2 + \varepsilon_2{}^2)^{1/2}}{2}\right]^{1/2} \tag{7}$$

$$\kappa = \left[\frac{-\varepsilon_1 + (\varepsilon_1{}^2 + \varepsilon_2{}^2)^{1/2}}{2}\right]^{1/2} \tag{8}$$

Finally, the surface reflectivity R and absorption coefficient α can be determined using the Fresnel Equations:

$$R = \frac{(n-1)^2 + \kappa^2}{(n+1)^2 + \kappa^2} \tag{9}$$

$$\alpha = 4\pi f \kappa / c \tag{10}$$

where the c is the speed of light in a vacuum.

2.2. Measurement model for photoacoustic testing

In this section, the dynamic behavior of temperature-dependent properties is integrated into the measurement model of femtosecond photoacoustic testing, which includes ultrafast laser-matter interaction, the generation and propagation of acoustic waves, and acousto-optic detection.

During femtosecond photoacoustic testing, the ultra-short laser pulse excites only the electron system without significantly heating the lattice, leading to a non-equilibrium heating process. This distinct thermal response, resulting from the short duration of the laser pulse compared to the characteristic times between electron and lattice interactions, requires treating their temperature distributions as separate subsystems. The Two-Temperature Model (TTM) was proposed to describe this non-equilibrium heating process in ultrafast laser-matter interactions. The temporal and spatial evolution of the electron temperature (T_e) and the lattice temperature (T_l) are calculated according to TTM as follows[6]:

$$C_e(T_e)\frac{\partial T_e}{\partial t} = \frac{\partial}{\partial z}\left(\kappa_e \frac{\partial T_e}{\partial z}\right) - G(T_e - T_l) + Q \tag{11}$$

$$C_l(T_l)\frac{\partial T_l}{\partial t} = G(T_e - T_l) \tag{12}$$

where C is the heat specific, T is the temperature, κ is the thermal conductivity, G is the electron–lattice coupling factor, and Q is the volumetric laser heat source. The quantities with subscripts e and l are associated with the electrons and lattice, respectively. Eqs. (11) and (12) assume that heat transport in the electron and lattice systems follows the classical Fourier law, which is valid for laser pulses longer than several tens of femtoseconds. The duration of the light sources used in this work ranges from 107 to 276 fs. The diffusion term in Eq. (12) is ignored because the timescale of heat accumulation is significantly longer than that of single pulse irradiation.

The one-dimensional model of volumetric heat source generated by the laser energy deposition of a Gaussian laser beam in both time and space can be expressed as[9]:

$$Q(z,t) = \sqrt{\frac{\beta}{\pi}}\frac{(1-R)J_0}{t_p z_s[1-e^{-L/z_s}]}\exp\left[-\left(\frac{z}{z_s}\right) - \beta\left(\frac{t-2t_p}{t_p}\right)^2\right] \tag{13}$$

where R is the surface reflectivity, J_0 is the peak fluence (at $z = 0$) carried by laser pulse, t_p is the laser pulse duration defined as the full width at the half maximum (FWHM) intensity of a laser pulse, z_s is the optical penetration depth equal to the reciprocal of absorption coefficient (α), L is the film thickness, and $\beta = 4\ln 2$.

In addition to the optical properties, variations in thermophysical properties should also be considered during the ultrafast laser-matter interaction. As mentioned earlier, the laser intensity used in this work is kept low to avoid damage to the nanofilms. Based on preliminary calculations, the maximum electron temperature will be lower than 3200 K. In this situation ($K_B T_e \ll E_F$), the electron heat capacity can be written as[28]:

$$C_e(T_e) = C_0 \bullet T_e \tag{14}$$

where C_0 is reference specific heat of the electron. The electron thermal conductivity can be given by[19]:

$$\kappa_e(T_e, T_l) = \frac{1}{3}\bullet C_e \overline{v^2} \bullet \tau_e \tag{15}$$

$$\overline{v^2} \approx {v_F}^2 + 3K_B T_e/m_e \tag{16}$$

where $\overline{v^2}$ is the characteristic value of the electron velocity square and v_F is the Fermi velocity, given approximately by $v_F = \hbar k_F/m_{opt}$. According to the study by Lin and Zhigilei[13], the electron-lattice coupling factor G can be assumed to be constant during the testing process given the relatively low electron temperature.

In solid photoacoustic testing, the essence of acoustic waves is the thermoelastic stress and strain induced by the nonuniform heat distribution resulting from laser irradiation. Based on preliminary calculations, the variation in lattice temperature will remain much lower than the electron temperature. In this situation, the thermoelastic properties of the lattice system can be treated as constant. Therefore, the one-dimensional model for the generation and propagation of acoustic waves in isotropic materials can be expressed as[29]:

$$\rho\frac{\partial^2 u_z}{\partial t^2} = 3\frac{1-\upsilon_p}{1+\upsilon_p}B\frac{\partial^2 u_z}{\partial z^2} - 3B\alpha_T\frac{\partial T_l}{\partial z} \tag{17}$$

where ρ is the density, u_z is the displacement in z-axis, υ_p is the Poisson's ratio, B is the bulk modulus, and α_T is the thermal expansion coefficient. The thermoelastic strain distribution in this one-dimensional model can be given by $\eta_{zz} = \partial u_z/\partial z$.

In this work, we employ the time-delayed pump-probe technique to detect the high-frequency acoustic waves. These acoustic waves are detected by the probe pulse through measuring the relative change in surface reflectivity. It should be noted that both the pump pulse and the probe pulse are derived from the same laser source and share the same wavelength.

According to the study by Osamu Matsuda et al., the amplitude coefficient for the electric field affected by a small perturbation $\Delta\varepsilon = F\delta(z - z')$ corresponding to a strain pulse at a depth of z' under the nanofilm surface can be given by $r' = iFk^2/(2k_1)$, where $k_1 = k\tilde{n} = k(n + i\kappa)$ and k represents the free-space wave number. The total reflected electric field from the nanofilm surface can be written as [30]:

$$rE^{(0)} = \left(r_0 + \frac{iFk^2 t_0 \tilde{t_0}}{2k_1}e^{2ik_1 z'}\right)E^{(0)} \tag{18}$$

where r_0 is the reflection coefficient, t_0 and $\tilde{t_0}$ are the transmission coefficients determined by the Fresnel Equations: $r_0 = (1 - n - i\kappa)/(1 + n + i\kappa)$, $t_0 = 2/(1 + n + i\kappa)$, and $\tilde{t_0} = 2(n + i\kappa)/(1 + n + i\kappa)$, and $E^{(0)}$ is the initial electric field. The reflection coefficient for a general distribution of strain $\Delta\varepsilon(z)$ can be calculated by integrating such contributions:

$$r = r_0 + \frac{ik^2}{2k_1}t_0\tilde{t_0}\int_0^\infty \Delta\varepsilon(z')e^{2ik_1 z'}dz' \tag{19}$$

where the integral accounts for the contributions of strain at different depths z' within the nanofilm. The relative change in reflectance $\delta r = r - r_0$ induced by the propagating thermoelastic strain $\eta_{zz}(z', t)$ can be written as:

$$\frac{\delta r(t)}{r_0} = \frac{4ik\tilde{n}}{1-\tilde{n}^2}\left(\frac{dn}{d\eta_{zz}} + i\frac{d\kappa}{d\eta_{zz}}\right)\int_0^\infty \eta_{zz}(z', t)e^{2ik\tilde{n}z'}dz' \tag{20}$$

where $dn/d\eta_{zz}$ and $d\kappa/d\eta_{zz}$ are wavelength-dependent photoelastic constants. From the relative change in reflectivity given by $\delta R/R_0 = 2\mathrm{Re}(\delta r/r_0)$, the Eq. (20) can be simplified to[31]:

$$\delta R(t) = \int_0^\infty f(z)\eta_{zz}(z, t)dz \tag{21}$$

$$f(z) = f_0\left[\frac{dn}{d\eta_{zz}}\sin\left(\frac{4\pi nz}{\lambda} - \Psi\right) + \frac{d\kappa}{d\eta_{zz}}\cos\left(\frac{4\pi nz}{\lambda} - \Psi\right)\right]e^{-z/z_s} \tag{22}$$

where $f_0 = 8\frac{\omega[n^2(n^2+\kappa^2-1)+\kappa^2(n^2+\kappa^2+1)]^{1/2}}{c[(n+1)^2+\kappa^2]}$, and $\Psi = \arctan\left(\frac{\kappa(n^2+\kappa^2+1)}{n(n^2+\kappa^2-1)}\right)$. In the dynamic measurement model, the temperature-dependent optical properties in Eq. (22) are calculated using the Critical Point Model (CPM) to account for the effects of temperature variations.

3. Results and discussion

3.1. Fitting results of critical point models

As mentioned in Section 2, we used the simulated annealing method to determine the parameters in Eq. (3) for copper and AlCu nanofilms. For copper, we selected three oscillators based on previous studies, which demonstrated that this number provides satisfactory fitting accuracy for Cu[22]. Since AlCu is a more complex alloy, additional oscillators were needed to improve the fitting accuracy of the CPM. It is important to note that while increasing the number of oscillators could further enhance the fitting accuracy—since, theoretically, any line shape can be modeled with enough oscillators—this would introduce "artificial" transitions that do not correspond to actual physical processes[19]. As a result, the parameters would lose their physical significance. Therefore, we settled on four terms for AlCu, as this provides an optimal balance between fitting accuracy and maintaining a physically meaningful model. The resulting parameters for copper (with $\tau_e =$ 34.0 fs at room temperature) and AlCu (with $\tau_e = 8.0$ fs at room temperature) are listed in Table 1 and Table 2, respectively.

In Fig. 2, the optical properties (surface reflectivity and absorption coefficient) calculated by the CPM for copper and AlCu nanofilms are compared with experimental data[32], along with the fitting results obtained by the traditional Drude model and the LDM. While the CPM generally shows better fitting accuracy at room temperature compared to the other models, there is a noticeable discrepancy for AlCu nanofilms in the 800–900 nm wavelength range. We attribute this difference to the more complex optical absorption behavior of AlCu material, as it is an alloy with more intricate characteristics than pure metals. Increasing the number of oscillators could potentially improve accuracy in this range. However, given the computational resources required to do so, we consider the fitting error within this specific wavelength range acceptable. Even with this discrepancy, the CPM model still provides a significantly better fit for the absorption coefficient compared to the traditional Drude model and the LDM.

For the function of ν_{e-ph}, according to the studies by Fisher et al. and Ren et al., the exact values of the material parameters in Eq. (5) are listed in Table 3.

Fig. 3 shows the calculated optical parameters of the nanofilm as a function of electron temperatures, with the lattice temperature fixed at 315 K (since the variation in lattice temperature during actual photoacoustic testing is far less than the variation in electron temperature, usually in the tens of K). Fig. 3(a) corresponds to the reflectivity and absorption coefficient of copper nanofilm for a 515 nm wavelength light source, and Fig. 3(b) corresponds to the reflectivity and absorption coefficient of AlCu nanofilm for a 920 nm wavelength light source. The selection of laser light source parameters is consistent with our experimental setup. As shown in Fig. 3, as the electron temperature increases, the surface reflectivity of the nanofilm decreases, while the absorption coefficient increases. This trend applies to both copper and AlCu films irradiated by different light sources.

Table 1
Parameters in critical point model tailored for copper nanofilms[18,22].

Parameter (units)	Value
ε_∞	3.686
ω_p (rad·s^{-1})	1.34×10^{16}
Γ (rad·s^{-1})	2.94×10^{13}
A_1	0.7435
ϕ_1	5.2686
ω_1 (rad·s^{-1})	3.5468×10^{15}
Γ_1 (rad·s^{-1})	5.5444×10^{14}
A_2	1.5222
ϕ_2	7.4936
ω_2 (rad·s^{-1})	9.3467×10^{15}
Γ_2 (rad·s^{-1})	2.5059×10^{14}
A_3	11.8746
ϕ_3	6.1984
ω_3 (rad·s^{-1})	4.2304×10^{14}
Γ_3 (rad·s^{-1})	1.0001×10^{14}

Table 2
Parameters in critical point model tailored for AlCu nanofilms[18].

Parameter (units)	Value
ε_∞	1
ω_p (rad·s^{-1})	2.39×10^{16}
Γ (rad·s^{-1})	1.25×10^{14}
A_1	644.4784
ϕ_1	−3.1136
ω_1 (rad·s^{-1})	4.2585×10^{14}
Γ_1 (rad·s^{-1})	1.6179×10^{12}
A_2	9.8110
ϕ_2	−0.3168
ω_2 (rad·s^{-1})	2.2874×10^{15}
Γ_2 (rad·s^{-1})	5.9060×10^{14}
A_3	170.8614
ϕ_3	−3.4664
ω_3 (rad·s^{-1})	9.3046×10^{14}
Γ_3 (rad·s^{-1})	3.4815×10^{15}
A_4	15.3988
ϕ_4	5.0673
ω_4 (rad·s^{-1})	2.7195×10^{15}
Γ_4 (rad·s^{-1})	2.3574×10^{15}

3.2. Results of temperature-dependent model

To understand the physical processes with dynamic properties and explore the influence of dynamic parameters during testing, numerical simulations are performed using the dynamic measurement model. The temperature distribution, stress distribution, and changes in surface reflectivity are calculated and visualized. These results are then compared with those obtained from the original model with constant parameters. Furthermore, the numerical results of $\delta R(t)$ are compared with experimental signals to validate the fitting accuracy of the proposed model.

The finite difference method (FDM) is used to solve the heat conduction equation and determine the temperature distribution in the nanofilms, while the finite element method (FEM) is employed to solve the momentum equation and calculate the stress and strain distribution. Both FDM and FEM share a numerical implementation with a time step of 2 fs and a grid size of 5 nm. A time step of 2 fs ensures accurate resolution of the ultrafast energy exchange dynamics between the electron and lattice systems. Under the selected experimental conditions, the electron relaxation time for AlCu nanofilms is ~ 8 fs at room temperature, decreasing to ~ 7 fs as the temperature increases. For copper nanofilms, the electron relaxation time is ~ 34 fs at room temperature, decreasing to ~ 20 fs with rising temperature. This reduction is attributed to a shift from electron-phonon to electron-electron collisions as the dominant relaxation mechanism at elevated temperatures[15]. In line with the Nyquist sampling theorem, a time step of 2 fs is sufficient to capture these ultrafast dynamics without introducing aliasing effects. The grid size of 5 nm was chosen to accurately resolve the acoustic waves generated by femtosecond laser pulses, which can have frequencies in the range of tens to hundreds of GHz. For a 100 GHz acoustic wave, the longitudinal velocity in metallic materials is ~ 5000 m/s, corresponding to a wavelength of around 50 nm. According to the Nyquist sampling theorem, a 5 nm grid size provides the necessary spatial resolution to capture the propagation of ultrasonic signals effectively while maintaining a balance between computational accuracy and resource efficiency. Additionally, based on the Courant–Friedrichs–Lewy (CFL) condition for the one-dimensional wave equation, the CFL value of the simulation model can be calculated as $s \bullet \Delta t/\Delta z \approx 0.002$, where s is the longitudinal velocity, Δt is the time

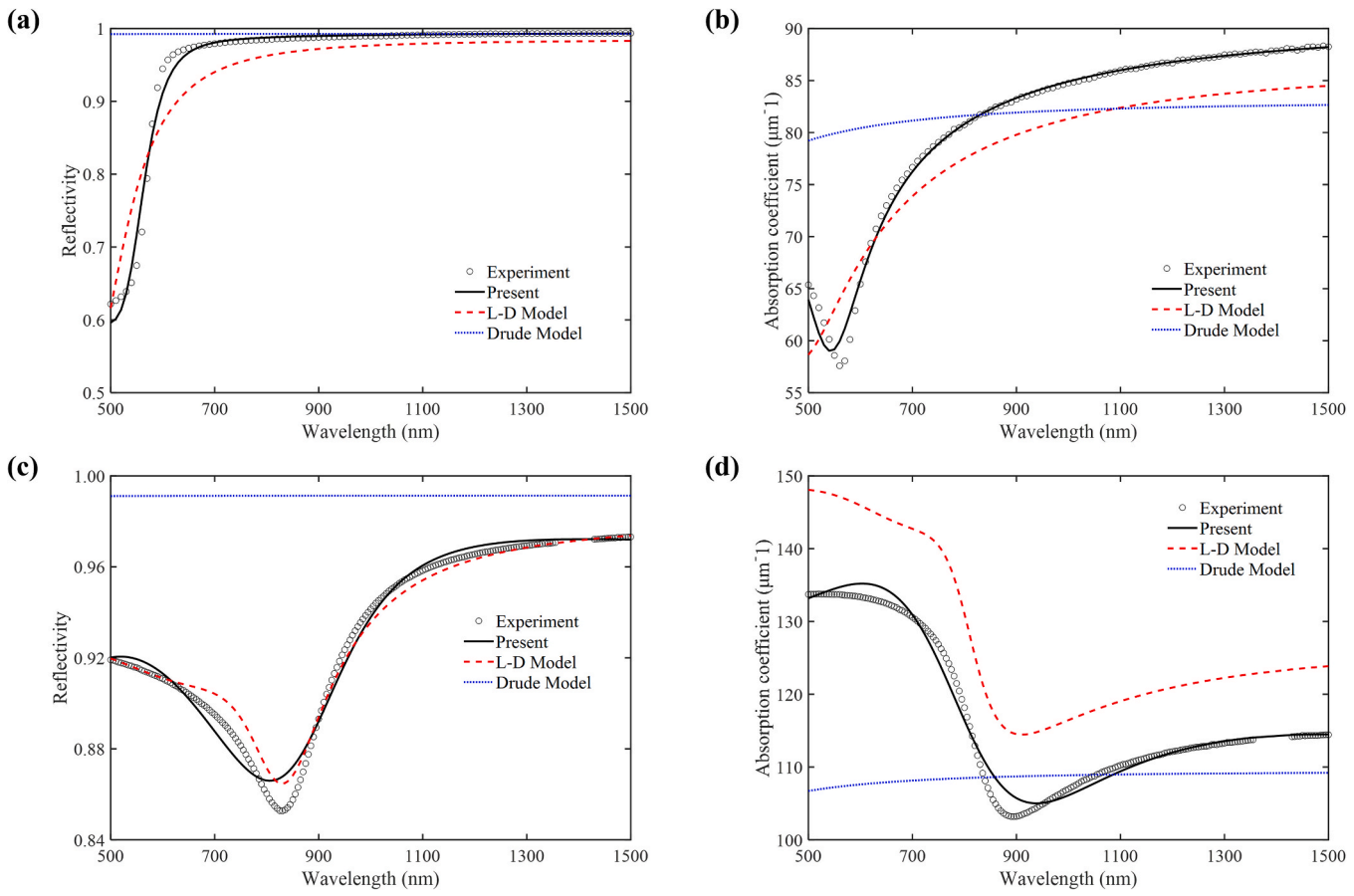

Fig. 2. (a) Reflectivity at room temperature versus wavelength calculated by different models for copper nanofilms (b) Absorption coefficient at room temperature versus wavelength calculated by different models for copper nanofilms (c) Reflectivity at room temperature versus wavelength calculated by different models for AlCu nanofilms (d) Absorption coefficient at room temperature versus wavelength calculated by different models for AlCu nanofilms.

Table 3
Parameters in ν_{e-ph} function for metal nanofilms[15,22].

Parameter (units)	Value for copper	Value for AlCu
Ξ (eV)	3.99	5.162
E_F (eV)	7	11.63
ρ (kg·m^{-3})	8960	2700
s (m·s^{-1})	5.01×10^3	6.42×10^3
m_{opt} (m_e)	1.39	1.20
q_b (m^{-1})	8.97×10^9	4.769×10^9

step, and Δz is the grid size. This CFL value is much smaller than 1, ensuring the stability and convergence of the numerical calculations [33].

For the FDM, the differential approximation uses a forward difference scheme for the temporal domain and a central difference scheme for the spatial domain. Regarding the boundary conditions, a Robin boundary condition is applied at the upper boundary to account for convective heat transfer between the nanofilm and air, while a Neumann boundary condition is used at the lower boundary to describe the continuity of heat flow between the nanofilm and the underlying material

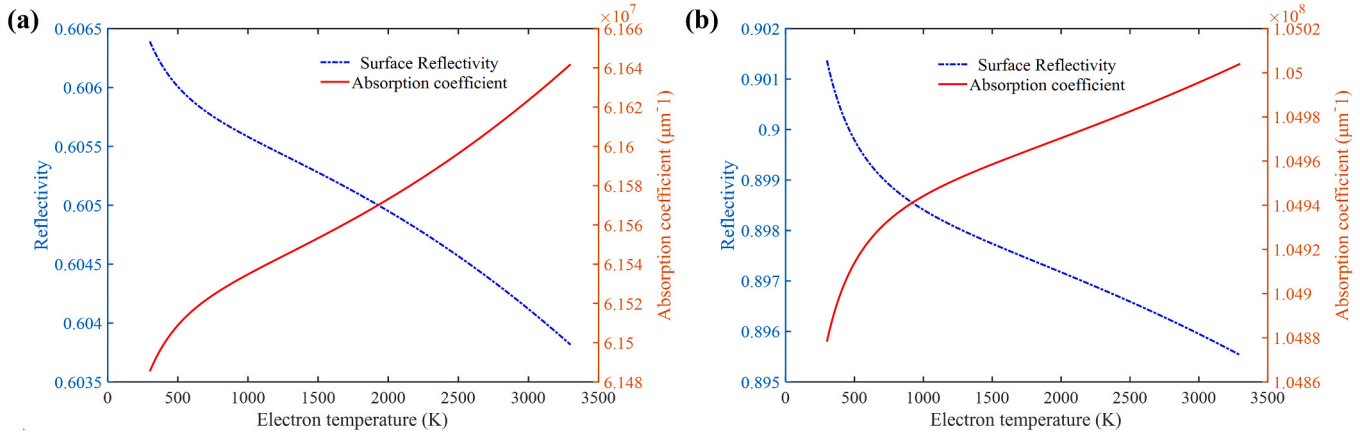

Fig. 3. (a) Reflectivity and absorption coefficient of copper nanofilms versus electron temperature for a 515 nm wavelength light source (b) Reflectivity and absorption coefficient of AlCu nanofilms versus electron temperature for a 920 nm wavelength light source.

Table 4
Laser parameters and material properties[13,28].

Parameter (units)	Value for copper	Value for AlCu
J_0 (J·m^{-2})	77	34
t_p (fs)	276	107
ω (rad·s^{-1})	3.66×10^{15}	2.05×10^{15}
C_0 (J·m^{-3}·K^{-1})	96.8	135
C_l (J·m^{-3}·K^{-1})	3.43×10^{6}	2.42×10^{6}
G	5.6×10^{16}	3.1×10^{17}
υ_p	0.34	0.35
α_T (K^{-1})	16.7×10^{-6}	23.1×10^{-6}
B	114.58×10^{9}	77.78×10^{9}
L (nm)	1000	500
Z (Pa·s·m^{-1})	42.66×10^{6}	17.33×10^{6}

[34].

For the FEM, the upper boundary is considered a free boundary, and the lower boundary includes an acoustic impedance model to compute the transmission and reflection of acoustic waves between the nanofilm and the underlying material. The reflection coefficient of acoustic waves can be given by $R_s = (Z_{in} - Z_{em})/(Z_{in} + Z_{em})$, where Z_{in} and Z_{em} represent the acoustic impedance of incident and emergent media, respectively [35]. The laser parameters and material properties used for numerical calculations are listed in Table 4.

The substrate material for both AlCu and copper nanofilms is silica glass. As an amorphous material, silica glass lacks the lattice and electronic system parameters characteristic of crystalline materials such as copper and AlCu. To avoid inconsistencies in the table's contents, the relevant parameters of silica glass are provided separately: a density of 2200 kg/m^3 , a longitudinal velocity of 5800 m/s, an acoustic impedance of 12.76×10^6 Pa·s/m, a thermal conductivity of 1.4 W/(m·K), a heat capacity of 1.54×10^6 J/(m^3·K), and a thickness of 5000 nm.

Figs. 4(a) and 4(b) illustrate the variations in surface reflectivity and absorption coefficient for copper nanofilms and AlCu nanofilms under femtosecond pulse irradiation, respectively. The normalized laser profiles are also shown. As depicted, during ultrafast laser-matter interaction, the surface reflectivity of the nanofilm rapidly decreases, while the absorption coefficient increases with rising electron temperature. These variations reach their peaks at 0.65 ps for copper nanofilms and 0.25 ps for AlCu nanofilms, correlating positively with the pulse duration of the light source (276 fs for copper and 107 fs for AlCu). Subsequently, as heat transfers from the electron system to the lattice system, the electron temperature decreases, causing the surface reflectivity to gradually rise and the absorption coefficient to gradually decrease.

Fig. 5 presents the temporal distribution of electron and lattice temperatures on the surface of the nanofilms as calculated by different models. The solid red line represents the dynamic model with dynamic optical properties, while the dashed blue line represents the original model with constant optical properties. The results show that both electron and lattice temperatures are higher when calculated with dynamic optical properties. For copper nanofilms, the maximum electron and lattice temperatures calculated with dynamic properties are 2215.1 K and 331.8 K, respectively, compared to 2043.6 K and 329.1 K for constant properties. For AlCu nanofilms, the maximum electron and lattice temperatures calculated with dynamic properties are 857 K and 315.5 K, respectively, compared to 846.8 K and 315.2 K for constant properties. The temperature rise in the copper film is significantly higher than in the AlCu film due to the higher laser fluence and lower reflectivity of copper at a wavelength of 515 nm compared to AlCu at 920 nm.

Fig. 6 shows the longitudinal stress profiles within the nanofilm at various times. The solid line indicates the acoustic pressure distribution calculated with dynamic properties, while the dashed line represents the distribution with constant properties. Fig. 6(a) and (b) reveal that as time progresses, the fluctuations and amplitude of acoustic pressure decrease and spread in the depth direction. The dynamic model shows higher stress values, reflecting a stronger thermal response due to the incorporation of temperature-dependent properties.

To validate the fitting accuracy of our model, we compared the numerical results with experimental signals. The experimental setup was based on a conventional pump-probe scheme. For the copper nanofilm, a laser source with a pulse duration of approximately 276 fs, a central wavelength of 515 nm, and a repetition rate of 54 MHz was used. For the AlCu nanofilm, the laser source had a pulse duration of about 107 fs, a central wavelength of 920 nm, and a repetition rate of 80 MHz. The laser output was split into pump and probe beams using a beam splitter. The pump beam was chopped at ~ 2 MHz by an acousto-optic modulator (AOM) for lock-in detection to improve the signal-to-noise ratio (SNR). An optical delay line was placed in the path of the probe beam to control the time delay between the pump and probe pulses before they reached the nanofilm surface. Both beams were focused onto the nanofilm surface, ensuring their spots overlapped. The pump beam was nearly perpendicular to the surface, with a spot size of 20 × 15 μm, corresponding to peak laser fluences of 77 J/m^2 for copper and 34 J/m^2 for AlCu. The probe beam was incident at ~ 45 degrees to the sample surface, resulting in a spot size of 10 × 8 μm, and the intensity of the reflected probe was measured by a photodetector. The lock-in amplifier used was the MFLI-5M (Zurich Instruments, Zurich, Switzerland). The photodetector bandwidths were 150 MHz (PDA10A2, Thorlabs, Newton, NJ, USA) for copper and 200 MHz (PDA200MA, Discoveryoptica, Beijing, China) for AlCu. This experimental setup achieved a time resolution of 12 fs, enabling precise measurements of ultrafast dynamics.

Fig. 7 displays the comparison between the numerical results of $\delta R(t)$

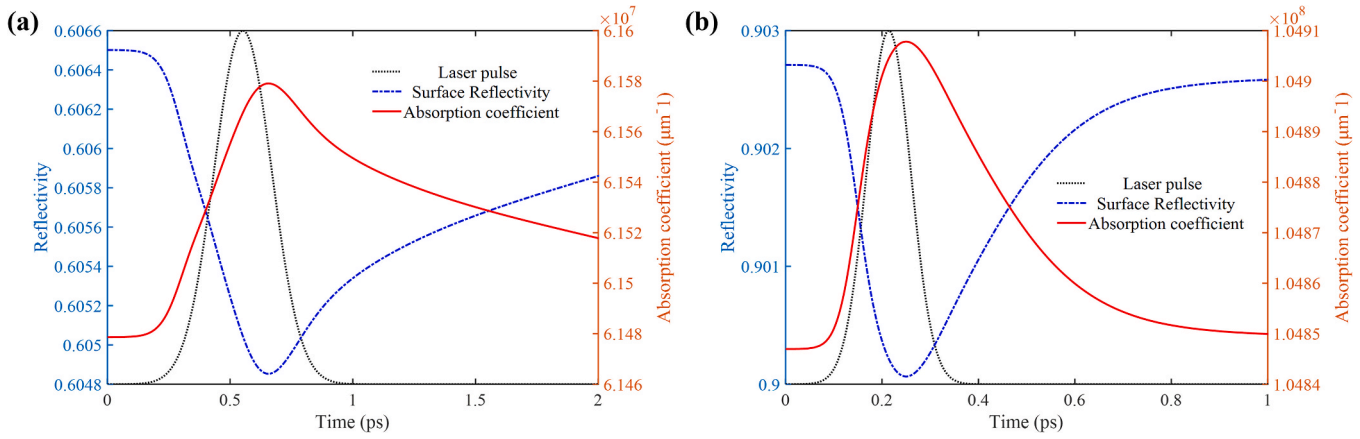

Fig. 4. (a) Variations of surface reflectivity and absorption coefficient of copper nanofilms under laser irradiation (b) Variations of surface reflectivity and absorption coefficient of AlCu nanofilms under laser irradiation.

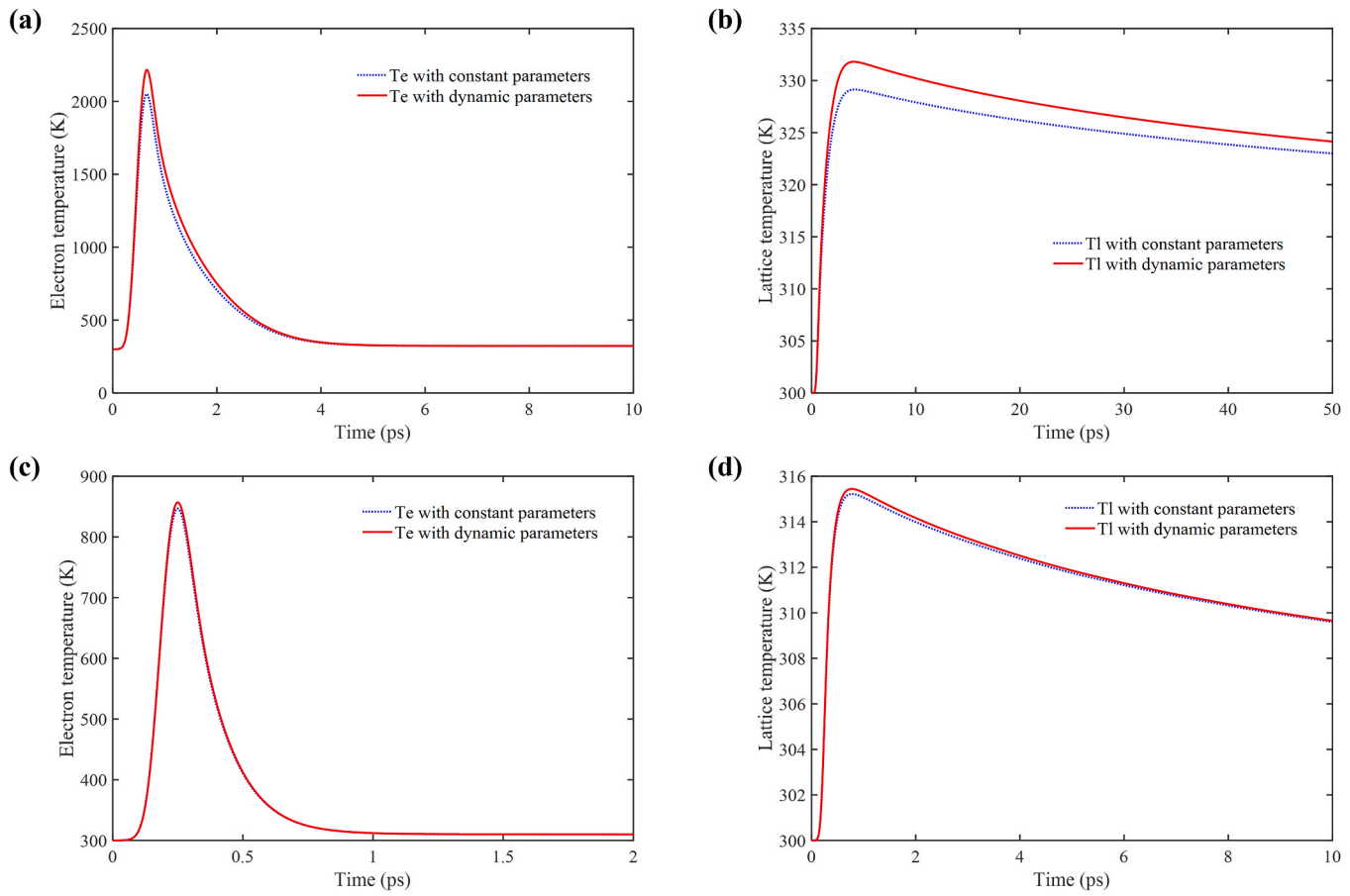

Fig. 5. (a) Temporal distribution of electron temperature in copper nanofilm calculated by different models (b) Temporal distribution of lattice temperature in copper nanofilm calculated by different models (c) Temporal distribution of electron temperature in AlCu nanofilm calculated by different models (d) Temporal distribution of lattice temperature in AlCu nanofilm calculated by different models.

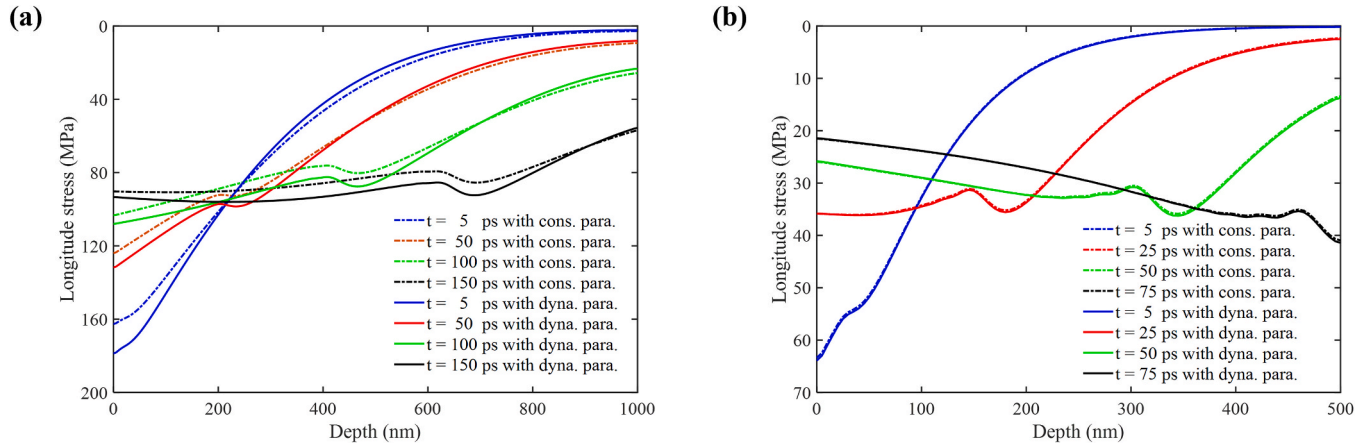

Fig. 6. (a) Profile of longitudinal stress in the copper nanofilm at various times calculated by different models (b) Profile of longitudinal stress in the AlCu nanofilm at various times calculated by different models.

obtained from the dynamic model and the experimental signals, alongside results from the original model. In both Fig. 7(a) and (b), the dynamic model shows improved agreement with the experimental data in the early stages compared to the original model with constant parameters. However, as the electron-lattice temperature stabilizes, the results from both constant and dynamic parameters become nearly identical. Between the initial peak and the second peak (the echo signal reflected from the lower boundaries of the nanofilm), discrepancies between the numerical and experimental results emerge, with the deviation being more pronounced in the copper nanofilms (Fig. 7(a)) than in the AlCu nanofilms (Fig. 7(b)).

These discrepancies can be attributed to three main factors. First, the simulation assumes ideal, homogeneous materials, while actual copper and AlCu nanofilms deviate from this idealization. Porosity, grain orientation differences, and surface roughness, which are common in films fabricated via magnetron sputtering[36], affect material properties

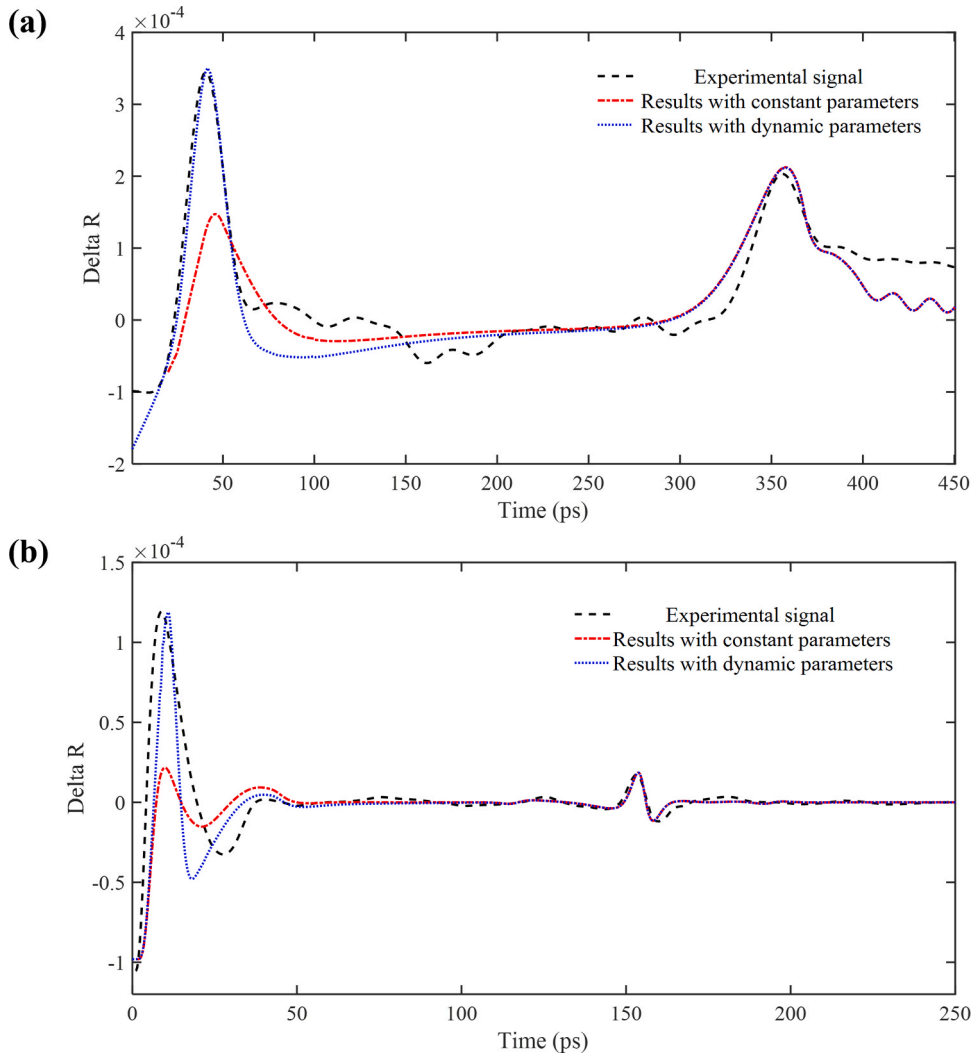

Fig. 7. (a) Comparison of experimental signal and simulated signal of the copper nanofilm calculated by different models (b) Comparison of experimental signal and simulated signal of the AlCu nanofilm calculated by different models.

and signal behavior. Porosity affects specific heat and thermal expansion uniformity[37]. It also increases acoustic wave scattering, which reduces the longitudinal wave velocity[38]. Grain orientation variation introduces anisotropy in bulk modulus and thermal expansion[39]. Surface roughness enhances light scattering, reducing reflectivity and increasing laser energy absorption[40]. Surface oxidation, inevitable during storage and measurement, further reduces reflectivity and increases energy absorption[41]. Second, the boundary conditions in the simulation are simplified for computational efficiency but differ from experimental reality. Surface roughness, oxidation, and interfacial defects between the nanofilm and substrate alter acoustic wave reflection and scattering behaviors, further contributing to deviations[42]. Third, unavoidable background noise contributes to the discrepancies. This effect is more pronounced in copper nanofilms because different laser sources were used for copper and AlCu to account for their distinct optical absorption characteristics. Copper nanofilms, which absorb more energy, exhibit larger deviations due to their higher excitation power.

The oscillations observed in the calculated curves, particularly for copper nanofilms in Fig. 7(a), provide additional insight into these discrepancies. Starting at approximately 370 ps, these oscillations are primarily caused by two factors. First, the higher energy absorption and longer electron relaxation time (~34 fs at room temperature) of copper lead to slower energy exchange between the electron and lattice systems. This prolonged relaxation generates sustained and intense acoustic waves, which interact and superimpose, producing the observed oscillations. Second, the free boundary condition applied at the upper boundary in the FEM model allows for complete reflection of acoustic waves without energy loss. As a result, these reflected waves interact with internal waves, further amplifying the oscillations. In contrast, AlCu nanofilms in Fig. 7(b), simulated using the same model, exhibit minimal oscillations due to lower absorbed energy and a shorter electron relaxation time (~8 fs at room temperature). This enables faster electron-lattice energy exchange and smoother acoustic wave dynamics. Moreover, the reflection coefficient between AlCu and silica glass (~0.15) is significantly lower than that between copper and silica glass (~0.54), resulting in much weaker reflected signals from the lower boundary[35]. This reduced reflection strength decreases the interaction between subsequent reflections at the upper boundary, further diminishing the observed oscillations.

In experimental signals, these oscillations are largely absent due to scattering and dissipation effects. Surface roughness induces multiple scattering events, randomizing the phase of reflected waves. Additionally, surface oxidation and internal defects, such as grain boundaries and porosity, dissipate acoustic energy during propagation, further suppressing oscillations. To better match experimental observations, we explored the application of partial absorbing boundary conditions to the upper boundary to simulate gradual dissipation of acoustic waves. This approach reduced the amplitude of reflected waves and significantly

mitigated the oscillation issue. However, determining the optimal absorption coefficient remains a challenge: an excessively high coefficient leads to the rapid disappearance of echo signals, weakening the reflective characteristics necessary for accurate simulation, while a low coefficient fails to sufficiently suppress oscillations. Further parameter analysis and experimental validation are required to refine the boundary conditions for improved agreement with experimental results.

Finally, we conducted a parameter sensitivity analysis to evaluate the influence of key factors on the photoacoustic signals. During the photothermal conversion phase, laser parameters (laser fluence, pulse duration, wavelength) determine energy absorption and heat distribution within the material[43]. In the thermoacoustic excitation phase, the electron-lattice coupling factor regulates energy transfer rates, while thermal expansion coefficients and bulk modulus influence thermal expansion and the intensity of the generated acoustic waves[13]. In the propagation phase, longitudinal sound velocity and acoustic impedance govern the propagation and reflection behaviors of the acoustic wave [35]. This analysis identified three critical parameters: laser parameters dictate the initial intensity of the photoacoustic signal; the electron-lattice coupling factor governs its initial signal shape; and the longitudinal wave velocity and acoustic impedance of nanofilms jointly determine the intensity, shape, and arrival time of the echo signal.

Despite the observed discrepancies, the dynamic model demonstrates significantly better agreement with experimental data compared to the original model, especially during the initial phase. This highlights the importance of incorporating temperature-dependent properties and dynamic behaviors into the measurement model for femtosecond photoacoustic testing of metal nanofilms.

4. Conclusions

In summary, this study presents the development and validation of a dynamic temperature-dependent measurement model for femtosecond photoacoustic testing of metal nanofilms. This model fully considers the dynamic behavior of temperature-dependent properties throughout the testing process, enhancing our understanding of the physical processes in ultrafast photoacoustic characterization. Initially, we proposed a CPM with three Lorentzian terms for copper and another with four Lorentzian terms for AlCu nanofilms to accurately describe the dynamic behavior of their optical properties under varying temperature conditions. Both models were validated by comparing the calculated optical properties with experimental data, demonstrating accurate fitting across wavelengths ranging from 500 to 1500 nm. Subsequently, we integrated the CPM into a comprehensive measurement model to account for dynamic processes throughout the testing. Numerical simulations of temperature distribution, stress distribution, and changes in surface reflectivity were performed. The dynamic model showed higher accuracy in predicting experimental outcomes for different materials under various light sources, confirming its ability to capture the dynamic behavior of metal nanofilms during ultrafast photoacoustic testing. The successful integration of CPM and TTM in the dynamic model paves the way for more accurate and efficient characterization techniques in the field of ultrafast laser-matter interactions.

Funding

This work was funded by the National Natural Science Foundation of China (52375541, 52130504, 52022034); Innovation Project of Optics Valley Laboratory (OVL2023PY003).

CRediT authorship contribution statement

Zhongyu Wang: Writing – original draft, Visualization, Validation, Software, Methodology, Investigation, Formal analysis, Data curation, Conceptualization. **Jing Min:** Investigation, Data curation. **Yong Sun:** Investigation. **Xuesong Wang:** Investigation. **Xiuguo Chen:** Writing – review & editing, Supervision, Resources, Funding acquisition. **Zirong Tang:** Writing – review & editing, Supervision, Resources, Project administration, Funding acquisition. **Shiyuan Liu:** Writing – review & editing, Supervision, Resources, Project administration, Funding acquisition.

Declaration of Competing Interest

The authors declare that they have no known competing financial interests or personal relationships that could have appeared to influence the work reported in this paper.

Acknowledgments

The authors would like to express their gratitude to Dr. Shihao Dong and Dr. Xinhao Zou from Shanghai Precision Measurement Semiconductor Technology, Inc. (PMISH) for their valuable contributions and insightful discussions related to this research.

Data availability

The authors do not have permission to share data.

References

[1] C. Thomsen, H.T. Grahn, H.J. Maris, J. Tauc, Surface generation and detection of phonons by picosecond light pulses, Phys. Rev. B 34 (6) (1986), https://doi.org/10.1103/PhysRevB.34.4129.
[2] D.H. Hurley, Pump-probe laser ultrasonics: characterization of material microstructure, IEEE Nanotechnol. Mag. (2019), https://doi.org/10.1109/MNANO.2019.2904772.
[3] K.Y. Chou, C.L. Wu, C.C. Shen, J.K. Sheu, C.K. Sun, Terahertz photoacoustic generation using ultrathin nickel nanofilms, J. Phys. Chem. C 125 (5) (2021) 3134–3142, https://doi.org/10.1021/acs.jpcc.0c09303.
[4] G.D. Tsibidis, Ultrafast dynamics of non-equilibrium electrons and strain generation under femtosecond laser irradiation of Nickel, Appl. Phys. 124 (2018) 311, https://doi.org/10.1007/s00339-018-1907-1.
[5] J. Min, X. Chen, Z. Wang, J. Hu, Y. Sun, Z. Tang, S. Liu, Deep learning-based identification of characteristic regions for picosecond ultrasonics metrology, Measurement 218 (2023) 113205, https://doi.org/10.1016/j.measurement.2023.113205.
[6] S.I. Anisimov, B.L. Kapeliovich, T.L. Perel'Man, Electron emission from metal surfaces exposed to ultrashort laser pulses, J. Exp. Theor. Phys. (1974), https://doi.org/10.1134/1.568853.
[7] T.Q. Qiu, C.L. Tien, Femtosecond laser heating of multi-layer metals—I. Analysis. Int. J. Heat. Mass Transf. 37 (17) (1994) 2789–2797, https://doi.org/10.1016/0017-9310(94)90055-8.
[8] T.Q. Qiu, T. Juhasz, C. Suarez, W.E. Bron, C.L. Tien, Femtosecond laser heating of multi-layer metals—II. Experiments. Int. J. Heat. Mass Transf. 37 (17) (1994) 2799–2808, https://doi.org/10.1016/0017-9310(94)90056-6.
[9] J.K. Chen, J.E. Beraun, D.Y. Tzou, Thermomechanical response of metal films heated by ultrashort-pulsed lasers, J. Therm. Stress. 25 (6) (2002) 539–558, https://doi.org/10.1080/01495730290074513.
[10] J.K. Chen, J.E. Beraun, L.E. Grimes, D.Y. Tzou, Modeling of femtosecond laser-induced non-equilibrium deformation in metal films, Int. J. Solids Struct. 39 (12) (2002) 3199–3216, https://doi.org/10.1016/S0020-7683(02)00175-2.
[11] S.I. Anisimov, B. Rethfeld, Theory of ultrashort laser pulse interaction with a metal, SPIE 3093 (1997) 192, https://doi.org/10.1117/12.271674.
[12] Migdal, K.P., Petrov, Y.V., Nitsky II, D.K., Zhakhovsky, V.V., Inogamov, N.A., Khishchenko, K.V., Knyazev, D.V., & Levashov, P.R. (2016). Heat conductivity of copper in two-temperature state. Applied Physics A, 122(4), 1-5, https://doi.org/10.1007/s00339-016-9870-5.
[13] Z. Lin, L.V. Zhigilei, Electron-phonon coupling and electron heat capacity of metals under conditions of strong electron-phonon nonequilibrium, Phys. Rev. B 77 (2008) 075133, https://doi.org/10.1103/PhysRevB.77.075133.

[14] G.L. Eesley, Generation of nonequilibrium electron and lattice temperatures in copper by picosecond laser pulses, Phys. Rev. B 33 (1986) 2144, https://doi.org/10.1103/PhysRevB.33.2144.
[15] D. Fisher, M. Fraenkel, Z. Henis, E. Moshe, S. Eliezer, Interband and intraband (Drude) contributions to femtosecond laser absorption in aluminum, Phys. Rev. E 65 (2001) 016409, https://doi.org/10.1103/PhysRevE.65.016409.
[16] D. Fisher, M. Fraenkel, Z. Zinamon, Z. Henis, E. Moshe, Y. Horovitz, E. Luzon, S. Maman, S. Eliezer, Intraband and interband absorption of femtosecond laser pulses in copper, Laser Part. Beams 23 (2005) 391–393, https://doi.org/10.1017/S0263034605230267.
[17] C.J. Powell, Analysis of optical and inelastic-electron-scattering data II. Application to Al, J. Opt. Soc. Am. 60 (1970) 78–93, https://doi.org/10.1364/JOSA.60.000078.
[18] A.D. Rakic, A.B. Djurisic, J.M. Elazar, M.L. Majewski, Optical properties of metallic films for vertical-cavity optoelectronic devices, Appl. Opt. 37 (1998) 5271, https://doi.org/10.1364/AO.37.005271.
[19] P.G. Etchegoin, E.C. Le Ru, M. Meyer, An analytic model for the optical properties of gold, J. Chem. Phys. 125 (2006) 164705, https://doi.org/10.1063/1.2360270.
[20] G.D. Tsibidis, The influence of dynamical change of optical properties on the thermomechanical response and damage threshold of noble metals under femtosecond laser irradiation, J. Appl. Phys. 123 (8) (2018) 085903, https://doi.org/10.1063/1.5020323.
[21] A. Vial, T. Laroche, Comparison of gold and silver dispersion laws suitable for FDTD simulations, Appl. Phys. B 93 (1) (2008) 139–143, https://doi.org/10.1007/s00340-008-3202-4.
[22] Y. Ren, J.K. Chen, Y. Zhang, Optical properties and thermal response of copper films induced by ultrashort-pulsed lasers, J. Appl. Phys. 110 (2011) 113102, https://doi.org/10.1063/1.3662897.
[23] J. Bonse, J. Krüger, Structuring of thin films by ultrashort laser pulses, Appl. Phys. A 129 (2023) 14, https://doi.org/10.1007/s00339-022-06229-x.
[24] Q. Yao, L. Guo, V. Iyer, X. Xu, Ultrafast electron–phonon coupling at metal-dielectric interface, Heat. Transf. Eng. 40 (13–14) (2018) 1211–1219, https://doi.org/10.1080/01457632.2018.1457281.
[25] J. Leng, J. Opsal, H. Chu, M. Senko, D.E. Aspnes, Analytic representations of the dielectric functions of materials for device and structural modeling, Thin Solid Films 313–314 (1998) 132, https://doi.org/10.1016/S0040-6090(97)00957-5.
[26] P.Y. Yu, M. Cardona, Fundamentals of Semiconductors: Physics and Materials Properties, Springer, 2004, https://doi.org/10.1007/978-3-540-27059-5.
[27] S. Kirkpatrick, C.D. Gelatt Jr., M.P. Vecchi, Optimization by simulated annealing, Science 220 (1983) 671–680, https://doi.org/10.1126/science.220.4598.671.
[28] C. Kittle, Introduction to Solid State Physics, John Wiles & Sons, 1967, https://doi.org/10.1119/1.1974239.
[29] E.G. Gamaly, The physics of ultra-short laser interaction with solids at non-relativistic intensities, Phys. Rep. 508 (4-5) (2011) 91–243, https://doi.org/10.1016/j.physrep.2011.02.001.
[30] O. Matsuda, M. Larciprete, R.L. Voti, O. Wright, Fundamentals of picosecond laser ultrasonics, Ultrasonics (2015), https://doi.org/10.1016/j.ultras.2014.09.004.
[31] G. Tas, H.J. Maris, Electron diffusion in metals studied by picosecond ultrasonics, Phys. Rev. B 49 (21) (1994) 15046–15054, https://doi.org/10.1103/PhysRevB.49.15046.
[32] K.M. McPeak, S.V. Jayanti, S.J.P. Kress, S. Meyer, S. Iotti, A. Rossinelli, D.J. Norris, Plasmonic films can easily be better: rules and recipes, ACS Photonics 2 (3) (2015) 326–333, https://doi.org/10.1021/ph5004237.
[33] R. Courant, K. Friedrichs, H. Lewy, On the partial difference equations of mathematical physics, IBM J. Res. Dev. 11 (2) (1967) 215–234, https://doi.org/10.1147/rd.112.0215.
[34] Y.A. Cengel, A.J. Ghajar. Heat and Mass Transfer: Fundamentals and Applications, fifth ed., McGraw-Hill, 2014.
[35] L. Kinsler, A. Frey, A. Coppens, J. Sanders, Fundamentals of Acoustics, Wiley, 2000.
[36] P. Panjan, A. Drnovšek, P. Gselman, M. Čekada, M. Panjan, Review of growth defects in thin films prepared by PVD techniques, Coatings 10 (5) (2020) 447, https://doi.org/10.3390/coatings10050447.
[37] X. Meng, L. Yan, J. Xu, F. He, H. Yu, M. Zhang, Effect of porosity and pore density of copper foam on thermal performance of the paraffin-copper foam composite phase-change material, Case Stud. Therm. Eng. 22 (2020) 100742, https://doi.org/10.1016/j.csite.2020.100742.
[38] R.J. Galvin, B. Gurevich, Effective properties of a poroelastic medium containing a distribution of aligned cracks, J. Geophys. Res. 114 (2009) 1–11, https://doi.org/10.1029/2008JB006032.
[39] N. Hansen, X. Huang, G. Winther, Effect of grain boundaries and grain orientation on structure and properties, Metall. Mater. Trans. A 42 (2011) 613–625, https://doi.org/10.1007/s11661-010-0292-5.
[40] J.M. Bennett, L. Mattsson, Introduction to Surface Roughness and Scattering, The Optical Society of America, 1999.
[41] R. Indhu, V. Vivek, L. Sarathkumar, A. Bharatish, S. Soundarapandian, Overview of laser absorptivity measurement techniques for material processing, Lasers Manuf. Mater. Process. 5 (2018) 458–481, https://doi.org/10.1007/s40516-018-0075-1.
[42] F.S. Hickernell, The acoustic properties of oxide films and their application to acoustic surface wave devices, J. Solid State Chem. 12 (1975) 225–231, https://doi.org/10.1016/0022-4596(75)90310-2.
[43] K. Kaleris, E. Kaniolakis-Kaloudis, E. Kaselouris, K. Kosma, E. Gagaoudakis, V. Binas, S. Petrakis, V. Dimitriou, M. Bakarezos, M. Tatarakis, N.A. Papadogiannis, Efficient ultrafast photoacoustic transduction on Tantalum thin films, Appl. Phys. A 129 (2023) 1–12, https://doi.org/10.1007/s00339-023-06797-6.

Zhongyu Wang received his Master's degree in optical engineering at China Academy of Engineering Physics (CAEP) in 2019. He is currently pursuing his Ph.D. degree at Huazhong University of Science and Technology (HUST). His research interests mainly focus on photoacoustic metrology for metal nanostructure.

Jing Min received her Bachelor's degree in Electrical Engineering at Wuhan University of Technology in 2018. She is currently pursuing her Ph.D. degree at Huazhong University of Science and Technology. Her research interests mainly focus on photoacoustic metrology technique for IC fabrication.

Yong Sun received his Master's degree in mechanical engineering at Huazhong University of Science and Technology (HUST) in 2024. His research interests mainly focus on Photothermal metrology technique for semiconductor.

Xuesong Wang born in 2000, graduated from Wuhan University of Technology in June 2022 with a bachelor's degree in engineering, and joined the Nano-optical Measurement Research Center of Huazhong University of Science and Technology in September of the same year. His research interests mainly focus on Photothermal metrology technique for semiconductor.

Xiuguo Chen is a professor of mechanical engineering at Huazhong University of Science and Technology. He received his B.E. in Mechanical Design Manufacturing and Automation from Shandong University of Technology in 2007, and M.E. and PhD in Mechanical and Electronic Engineering from Huazhong University of Science and Technology in 2009 and 2013, respectively. His research interests involve theory, instrumentation, and application of polarization-based techniques for nanoscale characterization and optical sensing.

Zirong Tang had been worked as an engineer in Silicon Valley, California till the end of 2004 since his Ph.D. graduation from University of California, Irvine in 2001, where his main responsibilities were developing novel optoelectronic devices and systems in Megasense Inc and Sensearray In. He joined Huazhong University of Science and Technology, Hubei, China as an associate professor in the School of Mechanical Science and Engineering in 2005 and was promoted to professor in 2010. His main research interests are in the area of micro/nanofabrication technologies and their applications.

Shiyuan Liu received the Ph.D. in mechanical engineering from Huazhong University of Science and Technology (HUST), Wuhan, China, in 1998, and worked as a visiting scholar at University of Manchester, Manchester, UK, from 2000 to 2001. He is currently a professor in School of Mechanical Science and Engineering at HUST. His research interests are computational imaging and computational lithography, micro/nano measurement technology and instrumentation, optical metrology and defect inspection for integrated circuit manufacturing, etc.